JOURNAL OF AIRCRAFT
Vol. 37, No. 1, January–February 2000

Direct Simulation of Acoustic Scattering by Two- and Three-Dimensional Bodies

Olivier A. Laik* and Philip J. Morris†
Pennsylvania State University, University Park, Pennsylvania 16802

A method is presented for the determination of acoustic scattering from two- and three-dimensional bodies with arbitrary geometries and in the presence of a nonuniform flow. The technique is an extension of the impedance mismatch method, in which the scattering body is replaced with a region of different acoustic impedance. To minimize the oscillations at the body surface, an auxiliary problem, related to the conservative form of the linearized Euler equations, is posed and solved numerically. Example problems are solved for a cylinder, a Rankine oval, and a sphere in a fluid at rest and in the presence of a nonuniform mean flow. Comparisons are made with exact solutions, if they are available, and the agreement between the numerical and the analytical solutions is very good.

Nomenclature

a	= speed of sound
b	= radius of sphere
D	= length of Rankine oval
d	= width of Rankine oval
$\boldsymbol{E}$, $\boldsymbol{F}$	= x, y components of flux
$H_0^{(2)}$	= zeroth-order Hankel function of second kind
k	= wavenumber
L	= smoothing parameter
M_x, M_y	= x, y components of Mach number
n	= distance normal to body surface
p	= pressure
Q	= source/sink strength
R	= reflection coefficient
$R_{\rho,n}$	= residual
r	= radial distance in cylindrical polar coordinates
r_0	= radial distance in spherical polar coordinates
t	= time
$\boldsymbol{U}$	= vector of unknown primitive variables
U, V, W	= x, y, z components of mean velocity
u, v	= x, y components of particle velocity
ρ	= density
ω	= frequency

Subscripts

i	= incident
n	= nonuniform mean flow in residual
o	= ambient properties
r	= reflected
s	= scattered
t	= transmitted
u	= uniform mean flow in residual
ρ	= value of mean density in residual
1, 2	= ambient properties of media 1, 2

Superscript

$\hat{}$	= auxiliary variable

Presented as Paper 98-2379 at the AIAA/CEAS 4th Aeroacoustics Conference, Toulouse, France, 2–4 June 1998; received 12 July 1998; revision received 2 July 1999; accepted for publication 3 July 1999.

*Graduate Research Assistant, Department of Aerospace Engineering. Student Member AIAA.

†Boeing/A. D. Welliver Professor, Department of Aerospace Engineering. Associate Fellow AIAA.

Introduction

RESEARCH on rotorcraft has generally been focused on increasing their speed and performance. This has drawn attention to the need to understand and control the noise that they generate. Various methods are available to predict the near and the far acoustic fields of rotorcraft. Ffowcs Williams and Hawkings[1] (FW-H) generalized Lighthill's acoustic analogy approach[2] including the effect of very general types of surfaces and surface motions. The FW-H equation is a rearrangement of the Navier–Stokes equation into an inhomogeneous wave equation with a quadrupole source distribution in the volume exterior to any surfaces and monopole and dipole sources on the surfaces.

The acoustic analogy has been used by Brentner[3] to develop the WOPWOP computer code that solves the FW-H equation for both near- and far-field noise. Recently Brentner[4] developed an efficient and robust method to predict high-speed impulsive noise by using a far-field approximation for the quadrupole source term. He implemented this technique in the WOPWOP+ code.

An alternative to the acoustic analogy approach is the direct computation of the flow and acoustic fields surrounding the rotor blades. This is simply the application of computational fluid dynamics (CFD) methodology to the calculation of the acoustic field directly as part of the unsteady fluid dynamic problem. Potential, Euler, or Navier–Stokes solvers have been used. The main drawback is that this numerical approach is very computationally time intensive. A large number of mesh points are required, and calculations quickly become too large, even for today's fastest computers. However, this direct method is potentially capable of providing the solution to the most complicated acoustic problems.

Nevertheless, calculations over limited regions can be extended to the far field by making use of Kirchhoff methods. The Kirchhoff formulation is based on an integration over a surface surrounding the rotor and allows both rotation and translation of this surface. Strawn et al.[5] compared the performance of rotating and nonrotating surfaces for Kirchhoff methods with experimental results and they showed good agreement. However, the inclusion of blade–vortex interaction noise prediction is not an easy task because the Kirchhoff surface is assumed to move through an environment at rest. Brentner and Farassat[6] have shown how the use of the FW-H equation can overcome many of the limitations associated with the linear Kirchhoff method. The major advantage of Kirchhoff and related methods over direct computations occurs in the far-field calculations. CFD solvers are generally applied to a limited domain, whereas the combined CFD/Kirchhoff method can compute the acoustic pressure at any location with reduced computational time requirements.

All these methods have advantages and some deficiencies, but usually they do not take into account the aircraft fuselage and wings

and the flow around the aircraft in their predictions. An obstacle in the path of a sound wave causes scattering and may be perceived as a secondary source of sound. These scattering effects cannot be ignored for sources near a scattering body, as is always the case for any powered aircraft.

Several methods have been developed to solve scattering problems from complex geometry bodies. These include the boundary and the finite element methods as well as finite difference approaches. Generally, these types of formulation cannot handle cases in which the acoustic source has a broad spectrum or in the presence of a nonuniform flow. Also, few studies have attempted a time-domain formulation of this phenomenon.

Hanson and Magliozzi[7] have developed a three-dimensional method in which the flowfield is made up of a boundary-layer region and an outer region free of shear. They consider the scattering of propeller noise by a fuselage modeled as an infinite cylinder. The acoustic waves are solved separately in each domain, and a matching condition is applied at the outer limit of the boundary layer. Previously, Hanson[8] had developed a helicoidal surface theory that gives the harmonic noise of propellers in the far field. Because of the presence of the fuselage, the free field predictions need to be corrected by factors varying from −20 to 4 dB in the flight direction. Also, a shadow zone occurs around the fuselage.

Another approach to scattering problems is the geometric acoustics (GA) method. Atalla and Glegg[9] have used a combination of geometric acoustics and the paraxial ray approximation (PRA). Results for the scattering of sound from a point source by a cylinder and by a Rankine oval show good qualitative agreement with the results of Hanson and Magliozzi. Atalla and Glegg[10] also applied the PRA to the problem of fuselage scattering of rotor noise. This GA method fails in the shadow zone where diffraction effects are important. Also, the specification of a more complicated scattering body shape than the ellipsoids and the rectangular boxes used in their model problems would be complicated.

The present study uses a new technique for the solution of time-dependent acoustic-scattering problems: the impedance mismatch method (IMM). This technique, developed by Chung,[11] simplifies the implementation of a solid wall boundary condition by setting the acoustic impedance of each medium encountered by the wave to a different value. This impedance difference results in reflected and transmitted waves with appropriate amplitudes. The primary benefit of this method is that no modifications to a simple Cartesian grid need to be made for complicated body geometries. Thus high-order finite difference schemes, suitable for computational aeroacoustics (CAA) simulations, may be applied without modification in all parts of the domain. Further details of the original implementation are given by Chung[11] and Chung and Morris.[12]

This paper introduces some major modifications to the IMM. First, it allows for the separate calculation of the incident field. This can be obtained from an analytical solution in the case of model problems or from a numerical prediction scheme such as WOPWOP+. Also, the method has been extended to include the effects of a nonuniform flow about the scattering body. This paper provides a validation of the method through the use of two- and three-dimensional model problems for which exact solutions exist, although this is not the case when nonuniform flow is included. A parallel program, written in Fortran 90, is used for the simulations. The ultimate goal of this work is to couple a rotorcraft noise prediction code, such as WOPWOP,[3] to this parallel scattering code to predict the noise scattered by the fuselage of a rotorcraft.

In the next section descriptions of the IMM, the governing equations, and the numerical implementation are given. Then several numerical simulations for acoustic scattering by two- and three-dimensional bodies are described. These include the scattering of sound from a line source by a cylinder and by a Rankine oval in a fluid at rest and in a nonuniform mean flow. Also considered are the scattering of waves from a point source by a sphere in a fluid at rest and in a nonuniform mean flow.

The examples presented here represent relatively low-frequency problems. The application of the present method to a typical rotorcraft application is given in the Discussion and Conclusions section. Also discussed is the application of the present method to scattering from bodies with sharp edges.

Impedance Mismatch Method

Basic Principle

The IMM is based on the propagation of acoustic waves in inhomogeneous media. Consider a plane interface between two media. The unperturbed properties of the media and the fluctuations in the two media are denoted by subscripts 1 and 2. Thus ρ_1 and ρ_2 are the mean densities and a_1 and a_2 are the speeds of sound in the two media, respectively. The incident wave impinges on the boundary between the two media, and this results in transmitted and reflected waves. In terms of the characteristic impedances of each medium ρa, the transmission and the reflection coefficients can be shown to be

$$T = \left|\frac{p_t}{p_i}\right| = \frac{2\rho_1 a_1}{\rho_1 a_1 + \rho_2 a_2} \tag{1}$$

$$R = \left|\frac{p_r}{p_i}\right| = \frac{\rho_2 a_2 - \rho_1 a_1}{\rho_1 a_1 + \rho_2 a_2} \tag{2}$$

where p_i, p_t, and p_r are the incident, transmitted, and reflected pressures, respectively.

Now consider the form of the linearized Euler equations for one-dimensional flow:

$$\frac{\partial \rho}{\partial t} + \rho_o \frac{\partial u}{\partial x} = 0 \tag{3}$$

$$\frac{\partial u}{\partial t} + \frac{1}{\rho_o}\frac{\partial p}{\partial x} = 0 \tag{4}$$

$$\frac{\partial p}{\partial t} + \rho_o a_o^2 \frac{\partial u}{\partial x} = 0 \tag{5}$$

where ρ_o and a_o are the densities and the speeds of sound in either medium. It should be noted that the discontinuities in the properties of the two media at the interface are matched by discontinuities in the spatial derivatives of the acoustic fluctuations. In this way the time derivatives are continuous. However, high-order spatial finite difference schemes have difficulty in the accurate approximation of such discontinuities. In fact, Chung[11] found that the numerical solutions to a naive application of the impedance mismatch concept exhibited instabilities. To overcome this problem, an auxiliary problem is solved. The one-dimensional auxiliary problem with no mean flow is described by the following set of equations, where $\hat{\rho} = \rho/\rho_0$, $\hat{u} = u\rho_0$, and $\hat{p} = p/\rho_0$:

$$\frac{\partial \rho}{\partial t} + \frac{\partial \hat{u}}{\partial x} = 0 \tag{6}$$

$$\frac{\partial u}{\partial t} + \frac{\partial \hat{p}}{\partial x} = 0 \tag{7}$$

$$\frac{\partial p}{\partial t} + a_o^2 \frac{\partial \hat{u}}{\partial x} = 0 \tag{8}$$

where the new dependent variables are required to be continuous at the interface. These new variables implicitly include the matching of discontinuities present in the physical problem. In the present analysis it is assumed that the speeds of sound are the same in the two media. This means that, in multidimensional problems, oblique waves are not distorted and the impedances of the two media are determined by their density. The transmission and the reflection coefficients then become

$$\hat{T} = |\hat{p}_t/\hat{p}_i| = 2\rho_2/(\rho_1 + \rho_2) \tag{9}$$

$$\hat{R} = |\hat{p}_r/\hat{p}_i| = (\rho_1 - \rho_2)/(\rho_1 + \rho_2) \tag{10}$$

Consequently, to represent the presence of a reflecting body a lower relative density, $\rho_2 \ll \rho_1$ is required. $\rho_2/\rho_1 = 1/30$ has been found to be an appropriate value to represent the density of the scattering body.[11] Now the solution in the first medium, outside the scattering body, is identical to the physical solution, whereas the solution inside the body is ficticious.

Thus, in the IMM, the presence of a body is represented by a lower mean density in governing equations. A body-fitted grid is not required and the same Cartesian grid may be used to represent any body geometry. The governing equations are described next.

Governing Equations

In the two-dimensional case, the total fluctuations satify the linearized Euler equations in nondimensional form:

$$\frac{\partial \boldsymbol{U}}{\partial t} + \underbrace{\frac{\partial \boldsymbol{E}}{\partial x} + \frac{\partial \boldsymbol{F}}{\partial y}}_{-R_{\rho_o,n}(\boldsymbol{U},t)} = 0 \tag{11}$$

where $\boldsymbol{U}$, $\boldsymbol{E}$, and $\boldsymbol{F}$ are defined by

$$\boldsymbol{U} = \begin{bmatrix} \rho \\ u \\ v \\ p \end{bmatrix}, \qquad \boldsymbol{E} = \begin{bmatrix} M_x\rho + \rho_o u \\ M_x u + p/\rho_o \\ M_x v \\ M_x p + \rho_o u \end{bmatrix}$$

$$\boldsymbol{F} = \begin{bmatrix} M_y\rho + \rho_o v \\ M_y u \\ M_y v + p/\rho_o \\ M_y p + \rho_o v \end{bmatrix} \tag{12}$$

and M_x and M_y are the nondimensional mean flow velocities in the x and the y directions, respectively. The velocity scale is the uniform speed of sound, the density scale is the density in the fluid medium ρ_1, and the length scale is based on a dimension of the scattering body as defined below. $R_{\rho_o,n}(\boldsymbol{U},t)$ denotes the residual. The first subscript indicates the value of the mean density and the second denotes whether the mean flow is uniform u or nonuniform n. The arguments of the residual are the vector of unknowns and note that the residual is time dependent.

The original IMM[11] solved for the total field. This would mean that an externally determined incident field would have to be imposed at one boundary of the computational domain. In addition, the same boundary would have to permit the radiation of scattered waves without reflection. The present implementation separates the incident and the scattered fields. In all the cases to be solved, the incident pressure is assumed to be known. This is either from an analytical solution or from a separate noise prediction code. All variables are split in three parts: a known unperturbed flow condition, denoted by the subscript o, a known incident perturbation, denoted by the subscript i, and an undetermined scattered perturbation, denoted by the subscript s. Thus,

$$\rho = \rho_o + \rho_i + \rho_s, \qquad u = U_o + u_i + u_s$$

$$v = V_o + v_i + v_s, \qquad p = P_o + p_i + p_s \tag{13}$$

Because many rotorcraft noise prediction codes predict only the acoustic pressure, only the incident pressure is assumed to be known. The particle velocities of the incident field are calculated.

The incident field is assumed to propagate in a uniform mean flow with components M_{xo} and M_{yo} in the x and the y directions, respectively. So it satisfies the equation

$$\frac{\partial \boldsymbol{U}_i}{\partial t} + \underbrace{\frac{\partial \boldsymbol{E}_i}{\partial x} + \frac{\partial \boldsymbol{F}_i}{\partial y}}_{-R_{1,u}(\boldsymbol{U}_i,t)} = 0 \tag{14}$$

where, as the notation for the residual implies, $\boldsymbol{E}_i$ and $\boldsymbol{F}_i$ are given by Eqs. (12) with $\rho_o = 1$, $M_x = M_{xo}$, $M_y = M_{yo}$, and $\boldsymbol{U} = \boldsymbol{U}_i$.

If the equation for the incident field is subtracted from the total field equation and the fluctuations are split into incident and scattered components, the equation for the scattered field may be written as

$$\frac{\partial \boldsymbol{U}_s}{\partial t} + \underbrace{\frac{\partial \boldsymbol{E}_s}{\partial x} + \frac{\partial \boldsymbol{F}_s}{\partial y}}_{-R_{\rho_o,n}(\boldsymbol{U}_s,t)} = -\left\{ \underbrace{\frac{\partial \boldsymbol{U}_i}{\partial t}}_{R_{1,u}(\boldsymbol{U}_i,t)} + \underbrace{\frac{\partial \boldsymbol{E}_i}{\partial x} + \frac{\partial \boldsymbol{F}_i}{\partial y}}_{-R_{\rho_o,n}(\boldsymbol{U}_i,t)} \right\} \tag{15}$$

or

$$\frac{\partial \boldsymbol{U}_s}{\partial t} = R_{\rho_o,n}(\boldsymbol{U}_s,t) + R_{\rho_o,n}(\boldsymbol{U}_i,t) - R_{1,u}(\boldsymbol{U}_i,t) \tag{16}$$

The first residual on the right-hand side of Eq. (16) represents the propagation of the scattered field in a nonuniform flow. The final two residuals represent the difference between the incident field in a uniform flow in the absence of the body and corrections for the nonuniform flow and the presence of the scattering body. These terms act as sources that drive the scattered field.

In the uniform medium, far from the body,

$$\frac{\partial \boldsymbol{U}_s}{\partial t} = R_{1,u}(\boldsymbol{U}_s,t) \tag{17}$$

That is, the right-hand side of Eq. (15) is equal to zero everywhere where the flow is undisturbed. This property of the governing equation is used to optimize the implementation. The incident field is calculated on only a smaller grid, a subset of the computational domain used for the scattered field.

Numerical Implementation

CAA requires a high accuracy in the numerical schemes used to obtain accurate numerical solutions with a minimum of dispersion and dissipation. Thus, the dispersion-relation-preserving finite difference scheme[13] has been used for the spatial discretization of these equations. The scheme uses a 7-point stencil and is formally fourth-order accurate: However, its dispersion characteristics are better than a sixth-order accurate, Taylor series-based scheme. The algorithm marches in time, and a time step consists of three calls to a fourth-order Runge–Kutta time-integration method for both fields. A new incident field is required at only the second and the fourth stages of the fourth-order Runge–Kutta time integration for the scattered field, as the source terms in the residual do not change between the second and the third stages. Therefore integration of the incident field is performed after the first and the third stages of the scattered-field integration. Nonreflecting boundary conditions[13] are applied at the boundary of both the incident and the scattered computational domains. In fact, because the incident pressure is already known, no particular boundary condition is required for letting the incident wave propagate out of the domain. Therefore the particle velocities at the outer points can simply be calculated from the Euler equations. Calculations with both the Euler equations and the nonreflecting boundary conditions have been performed and give similar results. However, the computational time is much lower when a radiation boundary condition is used.

The parallel programs are written in Fortran 90 and use the Message Passing Interface library for parallel communication. The computational domain consists of two grids: a large grid where the scattered field is calculated and a smaller grid where the particle velocities of the incident field are calculated. Both grids are Cartesian and are split evenly among the processors so that the workload of each processor is identical. Further details are given by Laik.[14]

The simulations have been performed on a Silicon Graphics Power Challenge with six processors for the two-dimensional cases and eight processors for the three-dimensional cases. The computational time depends on the size of both grids. For the case of scattering of a point source by a sphere at rest, 64.5 s per time step or 0.487 ms per time step per grid point is required. In the presence of the nonuniform mean flow the incident grid is larger and the computational time is higher: 82 s per time step or 0.625 ms per time step per grid point. Also, the two-dimensional simulations

show that the computational time scales linearly with the number of processors.

Two-Dimensional Simulations

This section presents a number of numerical examples of acoustic scattering by two-dimensional bodies. The results are compared with analytical solutions when they are available.

Plane Wave Impinging on a Cylinder

A plane wave propagates in the negative y direction and impinges on a cylinder of unit nondimensional radius with its axis perpendicular to the (x, y) plane located at the origin of the domain. The domains for the incident and the scattered fields are from $(x, y) = (-1.5, -1.5)$ to (1.5, 1.5) and from $(x, y) = (-5, -5)$ to (5, 5), respectively. A uniform Cartesian grid of 201 × 201 is used for the scattered field, with the cylinder diameter equal to 40 grid points. The domain is sketched in the Fig. 1. The effect of the body densities is perceived only in the vicinity of the cylinder. Therefore the incident particle velocities are calculated on only the smaller grid defined above.

The incident pressure is initialized with the following definition of a plane wave with a smoothed leading edge:

$$p_i(x, y, t) = \begin{cases} 0.01 \cos[k(y - y_{\text{source}}) + \omega t] \\ \qquad \text{for } y \geq y_{\text{source}} - t \\ 0.01 \exp\{-8[(y - y_{\text{source}} + t)^2]\} \\ \qquad \text{otherwise} \end{cases} \tag{18}$$

with

$$k = \omega = \pi, \qquad \rho_i(x, y, t) = p_i(x, y, t)$$
$$u_i(x, y, 0) = v_i(x, y, 0) = 0 \tag{19}$$

y_{source} is chosen so that there are no incident pressure disturbances inside the cylinder at the beginning of the simulation. Otherwise the time history is dominated by a transient disturbance. This transient is caused by the presence of an incident wave in the solid without any cancellation by the scattered field at the beginning of the calculation. It dominates the total pressure history and contaminates the results.

In this case, the use of a plane wave provides an easy way to evaluate the accuracy of the incident-wave particle velocity calculations. A comparison shows a good agreement everywhere except in a region near the computational boundaries, 5–6 points wide, where the relative error is greater than 10^{-6} and can reach 10%. This may be due to the incompatability of the asymptotic boundary conditions and a plane-wave solution. In any event, these boundary values are removed in the calculation of the scattered field in Eq. (16).

In the immediate vicinity of the body, high wave-number disturbances are noticeable and arise from the discontinuity of body densities at the interface. It should be noted that, although the new dependent variables in the auxiliary problem, $\hat{p}$, $\hat{u}$, $\hat{v}$, and $\hat{p}$, are continuous at the interface, their derivatives are not. To reduce the effect of this discontinuity, a model of the interface, which is commonly used in oceanography for the propagation of waves in layered media, is applied in this study. The jump in body densities is replaced with a smoothing function of the form

$$\rho_0 = \tfrac{1}{2}(1 + \tfrac{1}{30}) + \tfrac{1}{2}(1 - \tfrac{1}{30}) \tanh[(n - 1)/L] \tag{20}$$

where L is the distance over which the density changes from $\frac{1}{30}$ to 1 and n is the distance normal to the surface. A value of L of 0.05 has been used in the present calculations. A detailed study of the effect of this parameter has not been conducted, but smaller values would increase the generation of high wave-number disturbances and lower values would extend the influence of the body unrealistically. With the use of this smoothing of the surface discontinuity, the high wave-number disturbances at the interface vanish.

Figure 2 presents the rms pressure contours. As expected, the maximum reflections are located above the cylinder whereas the zone behind the body is shadowed. The IMM solution agrees very well with the analytic solution.[15] However, some differences are perceived in the region close to the cylinder because the transmission coefficient has a nonzero value. Two slices have been extracted from the two-dimensional instantaneous plots to compare the analytic and the computational solutions. The pressure along the axes $y = 0$ and $x = 0$ are represented in Figs. 3 and 4, respectively. The errors are not significant and decrease with distance from the cylinder.

Line Source Scattering by a Rankine Oval

This section defines the Rankine oval geometry and the flow around the solid. Then the results of the simulations are given. First, the Rankine oval is placed in an environment at rest. Then these results are compared with the case of the scattering of waves from a line source by a Rankine oval in a flow perturbed by the solid.

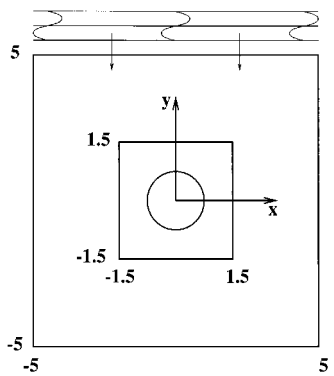

Fig. 1 Schematic of the computational domain for the scattering of a plane wave by a cylinder.

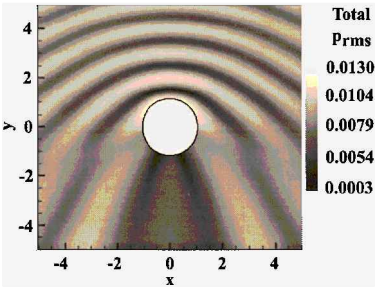

Fig. 2 Rms pressure for the scattering of a plane wave by a cylinder.

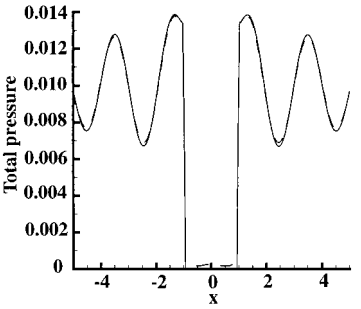

Fig. 3 Instantaneous pressure along the x axis at $t = 20$ for the scattering of a plane wave by a cylinder: ——, analytical solution; and - - -, numerical solution.

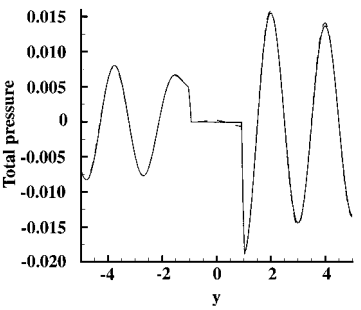

Fig. 4 Instantaneous pressure along the y axis at $t = 20$ for the scattering of a plane wave by a cylinder: ——, analytical solution; and - - -, numerical solution.

Geometry and Flow

The flow around the Rankine oval is determined by the superposition of a source and a sink of equal strength in a uniform flowfield. In the simulations, the nondimensional magnitude of the undisturbed flow is $M_{xo} = 0.4$. The strength of the source and the sink and the distance between them are $Q = 0.3811065$ and $2d = 1.4561566$, respectively. A Rankine oval of length $D = 2$ and width $d = 1$ is placed at the origin of the domain and the interface is smoothed, as in the cylinder case. Around the solid, the flow velocities in the x and the y directions may be written as

$$U(x, y) = U_o + \frac{Q(x + d)}{4\pi[(x + d)^2 + y^2]^{\frac{3}{2}}} - \frac{Q(x - d)}{4\pi[(x - d)^2 + y^2]^{\frac{3}{2}}}$$

$$V(x, y) = \frac{Qy}{4\pi[(x + d)^2 + y^2]^{\frac{3}{2}}} - \frac{Qy}{4\pi[(x - d)^2 + y^2]^{\frac{3}{2}}} \tag{21}$$

Inside the body, the flow velocity is set to zero.

No Mean Flow

A line source is placed at $(x, y) = (0, 2)$ and the incident acoustic waves impinge on the Rankine oval centered at the origin. The computational domains for the incident and the scattered fields are from $(x, y) = (-1.5, -1.5)$ to $(1.5, 1.5)$ and from $(x, y) = (-9, -9)$ to $(9, 9)$, respectively. A uniform Cartesian grid of 361×361 is used for the scattered field. The domain is sketched in Fig. 5.

The incident pressure is initialized with the following definition of a periodic wave from a line source:

$$p_i = (0.01/4i) \exp(i\omega t)\, H_0^{(2)}(kr) \tag{22}$$

where

$$k = \omega = \pi, \qquad \rho_i(x, y, t) = p_i(x, y, t)$$

$$u_i(x, y, 0) = v_i(x, y, 0) = 0 \tag{23}$$

and r is the radial distance from the source.

Until a stationary periodic solution is achieved, the pressure p_i is multiplied by a smoothing function of the form

$$\frac{1}{2}\left[1 - \tanh\left(\frac{r - X - ct}{0.05}\right)\right] \tag{24}$$

X is chosen so that the incident pressure is initially negligible inside the body.

Figure 6 shows the instantaneous pressure contours (the sum of the incident and the scattered fields) at time $t = 20$. The white oval shape represents the Rankine body. Also, a singularity exists at the location of the source, and this zone is masked by a white disk. The directivity pattern is symmetric about the y axis and consists of five lobes. This is shown in Fig. 7. A shadow zone lies behind the Rankine body, and behind the source the level of the sound is attenuated.

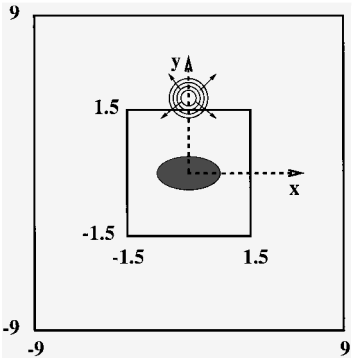

Fig. 5 Schematic of the computational domain for the scattering of waves from a line source by a Rankine oval.

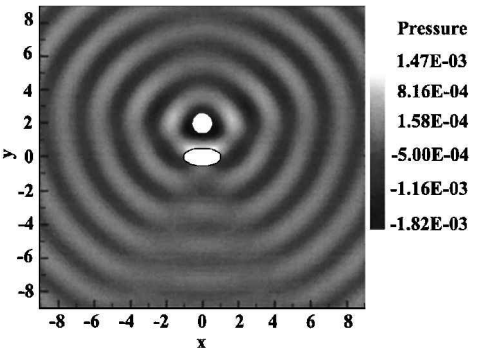

Fig. 6 Instantaneous pressure contour for the scattering of an acoustic wave from a line source by a Rankine oval at $t = 20$, $k = \pi$, and $M_x = 0$.

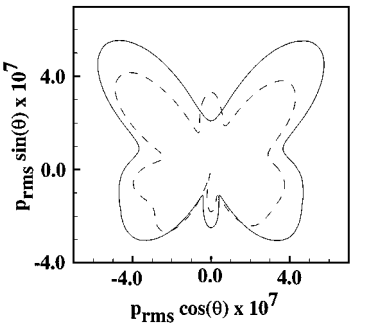

Fig. 7 Sound directivity for the scattering of an acoustic wave from a line source by a Rankine oval. $y_s = 2$, $k = \pi$: ——, $M_x = 0$; and – – –, $M_x = 0.4$.

Nonuniform Mean Flow

In this simulation, the Rankine oval is embedded in a fluid moving in the positive x direction and perturbed by the presence of the solid. In this case the line source is located at $(x, y) = (0, y_s) = (0, 10)$. This larger value is chosen to ensure that the mean flow is uniform in the vicinity of the source. The pressure distribution for an acoustic wave from a line source embedded in a fluid moving uniformly with a velocity U_o in the x direction may be written as

$$p(\boldsymbol{x}, t) = \frac{0.01}{4i(1 - M_x^2)^{\frac{1}{2}}} \exp\left\{\frac{i\omega}{1 - M_x^2}\left[t + \frac{(x - U_o t)U_o}{a_o^2}\right]\right\}$$

$$\times H_0^{(2)}\left\{\frac{\omega}{a_o(1 - M_x^2)}\left[x^2 + (1 - M_x^2)(y - y_s)^2\right]^{\frac{1}{2}}\right\} \tag{25}$$

with

$$M_x = U_o/a_o = 0.4, \qquad k = \omega = \pi, \qquad y_s = 10$$

$$\rho_i(x, y, t) = p_i(x, y, t), \qquad u_i(x, y, 0) = v_i(x, y, 0) = 0 \tag{26}$$

Also, the pressure is multiplied by the smoothing function given by expression (24) until a periodic state is achieved.

The computational domains for the incident and the scattered fields are from $(x, y) = (-6.5, -6.5)$ to $(6.5, 6.5)$ and from $(x, y) = (-9, -9)$ to $(9, 9)$, respectively. A uniform Cartesian grid of 381×381 is used for the scattered field. The grid for the incident field is much larger than that used in the preceding section. Because the mean flow is perturbed around the body, the grid borders have to be expanded so that the perturbations of the mean flow in both x and y directions at the edge of the incident domain are negligible.

Figure 8 shows the instantaneous pressure contours at time $t = 31.6$. The scattering pattern behind the Rankine body is seen clearly. In the region between the source and the solid a standing wave regime is established. The Doppler shift in wavelength is also evident.

Two other simulations have been performed in this case to show the effects of a mean flow on the scattering pattern: scattering in an environment at rest and in a uniform mean flow unperturbed

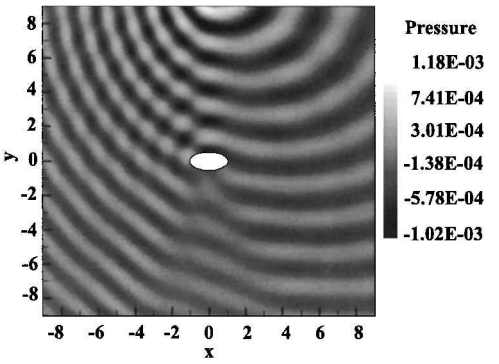

Fig. 8 Instantaneous pressure contour for the scattering of an acoustic wave from a line source embedded in a nonuniform mean flow by a Rankine oval at $t = 31.6$, $k = \pi$, and $M_x = 0.4$.

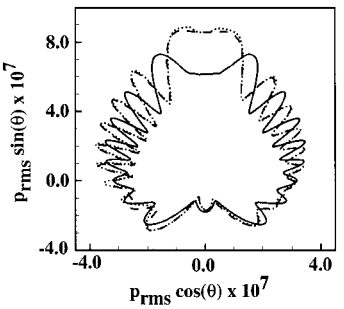

Fig. 9 Comparison of sound directivity patterns for the scattering of an acoustic wave from a line source by a Rankine oval. $y_s = 10$, $k = \pi$: ——, $M_x = 0$; – – –, $M_x = 0.4$, uniform flow; and ⋯, $M_x = 0.4$, nonuniform flow.

by the scattering body. The source and the solid are kept at the same locations. The directivity curves in Fig. 9 show the differences between these cases. The rms pressure is extracted on a circle of radius 5 centered at the origin. Therefore the patterns shown for $\sin\theta$ positive do not correspond to the far-field directivity because of the presence of the source at $(x, y) = (0, 10)$. The multiple lobes are associated with the interference between the incident and the scattered fields, as shown in Fig. 8. In all cases, the shadow zone remains almost identical. The mean flow shrinks this zone and tilts it backward slightly. The changes that are due to the nonuniformity of the mean flow do not appear to be important. This might not be the case for shapes other than a Rankine oval in which the mean flow nonuniformity could be greater.

In view of these small differences, a case in which the flow is assumed to be uniform has been simulated with the source located at $(x, y) = (0, 2)$. The comparison of far-field directivities, with and without flow, is shown in Fig. 7. There is a slight increase in the radiation upstream, as would be expected. It should be noted that the incident field has been modified by the presence of the mean flow so that the incident-pressure levels on the surface of the Rankine oval are not the same in the two cases shown in Fig. 7. This explains the reduction in the total field values in the presence of the mean flow.

Three-Dimensional Simulations: Point Source Scattering by a Sphere

This section presents two problems of acoustic scattering by three-dimensional bodies. First, results for the scattering of acoustic waves from a point source by a sphere are given and compared with the analytic solution.[16] Then the sphere is embedded in a nonuniform mean flow. No analytic solutions are available for the latter case.

No Mean Flow

A point source is placed at $(x, y, z) = (0, 2.5, 0)$ and the incident waves impinge on a sphere of radius $b = 0.5$ centered at the origin. The domains for the incident and the scattered fields are from $(x, y, z) = (-1.25, -1.25, -1.25)$ to $(1.25, 1.25, 1.25)$ and from $(x, y, z) = (-2.5, -2.5, -2.5)$ to $(2.5, 2.5, 2.5)$, respectively. A uniform Cartesian grid of $101 \times 101 \times 101$ is used for the

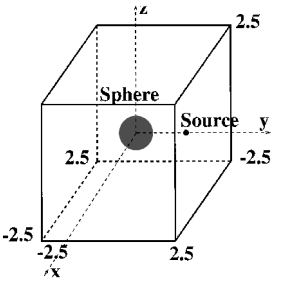

Fig. 10 Schematic of the computational domain for the scattering of an acoustic wave from a point source wave by a sphere.

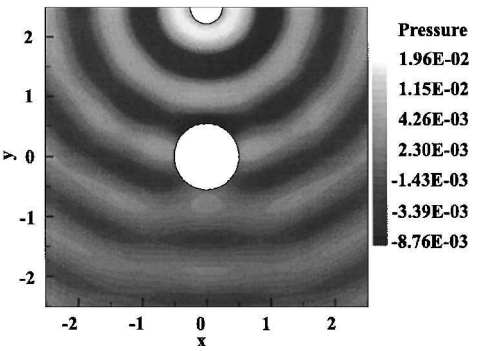

Fig. 11 Instantaneous pressure at $t = 8.5$ in the plane $z = 0$ for the scattering of an acoustic wave from a point source by a sphere. $k = 2\pi$ and $M_x = 0$.

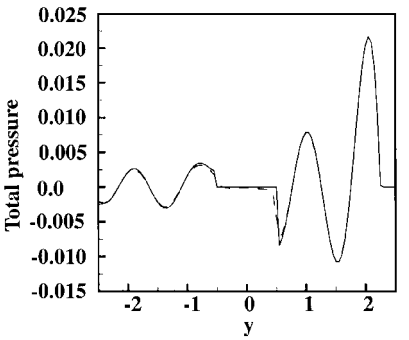

Fig. 12 Instantaneous pressure at $t = 8.5$ along the y axis for the scattering of an acoustic wave from a point source by a sphere. $k = 2\pi$ and $M_x = 0$: ——, analytical solution; and – – –, numerical solution.

scattered field. The domain is shown in Fig. 10. The incident pressure is initialized with the following definition of a point source:

$$\rho_i = 0.01[\cos(kr - \omega t)/r] \tag{27}$$

where

$$k = \omega = 2\pi, \qquad p_i(x, y, z, 0) = \rho_i(x, y, z, 0)$$

$$u_i(x, y, z, 0) = v_i(x, y, z, 0) = w_i(x, y, z, 0) = 0 \tag{28}$$

and r is the radial distance from the source. Until a periodic solution is achieved, the pressure p_i is multiplied by a smoothing function given by expression (24).

The wave number is given by $k = 2\pi$, so that $ka = \pi$, as in the two-dimensional simulations. Moreover, 20 points per wavelength are used. The Doppler effect increases the wave number at some locations in the presence of a mean flow. To be able to compare both simulations at rest and for $M_x = 0.4$, the number of points per wavelength must be kept higher than 5.

Figure 11 shows the instantaneous pressure contours at $t = 8.5$. The shadow zone can be seen behind the sphere on the y axis in Fig. 12. It also shows the good agreement between the analytic and the numerical solutions. Figure 13 shows a comparison between the analytic and numerical solutions on the z axis. The symmetry

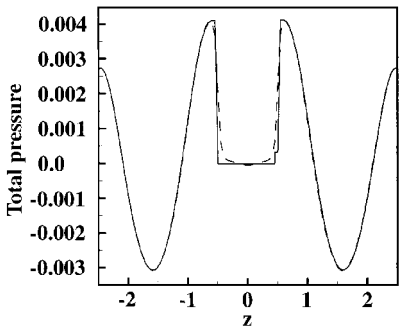

Fig. 13 Instantaneous pressure at $t = 8.5$ along the z axis for the scattering of an acoustic wave from a point source by a sphere. $k = 2\pi$ and $M_x = 0$: ——, analytical solution; and – – –, numerical solution.

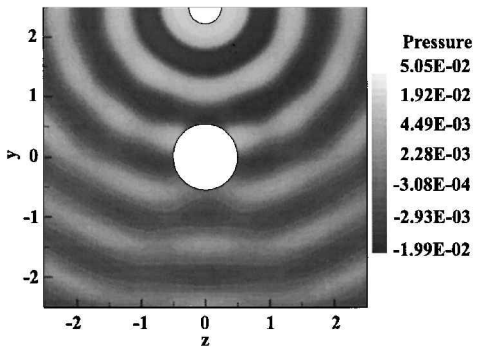

Fig. 14 Instantaneous pressure at $t = 8.5$ on the plane $x = 0$ for the scattering of an acoustic wave from a point source by a sphere. $k = 2\pi$ and $M_x = 0.4$.

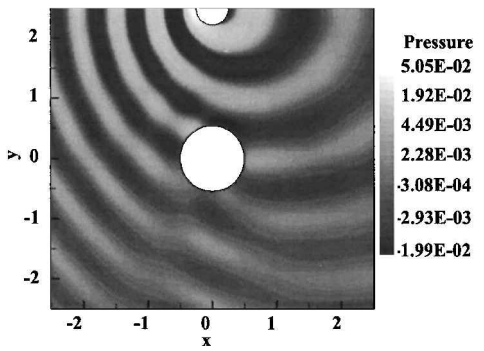

Fig. 15 Instantaneous pressure at $t = 8.5$ on the plane $z = 0$ for the scattering of an acoustic wave from a point source by a sphere. $k = 2\pi$ and $M_x = 0.4$.

and smoothness of the numerical solution and the good agreement between the analytic and numerical solutions can again be seen.

Nonuniform Mean Flow

A sphere of radius $b = 0.5$ and a point source are placed at the same locations, and the flow is described by

$$U(x, y, z) = \tfrac{1}{2}U_o\left[2 + b^3\left(1/r_o^3 - 3x^2/r_o^5\right)\right]$$

$$V(x, y, z) = -\tfrac{3}{2}U_o b^3 xy/r_o^5$$

$$W(x, y, z) = -\tfrac{3}{2}U_0 b^3 xz/r_o^5 \qquad (29)$$

where r_o is the distance from the center of the sphere. Inside the sphere the velocities are set to zero.

The domains for the incident and the scattered fields are from $(x, y, z) = (-1.75, -1.75, -1.75)$ to $(1.75, 1.75, 1.75)$ and from $(x, y, z) = (-2.5, -2.5, -2.5)$ to $(2.5, 2.5, 2.5)$, respectively. A uniform Cartesian grid of $101 \times 101 \times 101$ is used for the scattered field.

The incident pressure is initialized with the following solution for a point source in a fluid moving in the x direction at Mach number M_x:

$$p(\boldsymbol{x}, t) = \frac{0.01\exp(i\omega\tau^*)}{4\pi r\,[1 + M_x x/r]} \qquad (30)$$

where

$$\tau^* = t + \frac{M_x x/a_o - \left\{x^2 + (1 - M_x^2)\,[(y - 2.5)^2 + z^2]\right\}^{\frac{1}{2}}}{1 - M_x^2} \qquad (31)$$

$$k = \omega = 2\pi, \qquad p_i(x, y, z, 0) = \rho_i(x, y, z, 0)$$

$$u_i(x, y, z, 0) = v_i(x, y, z, 0) = w_i(x, y, z, 0) = 0 \qquad (32)$$

and r is the radial distance from the source.

Figures 14 and 15 show the instantaneous pressure contours at $t = 8.5$ in the $x = 0$ and the $z = 0$ planes, respectively. The solution is seen to be symmetric about the $z = 0$ plane in Fig. 14 and the shadow zone is also evident. Figure 15 shows how the shadow zone is tilted by the mean flow. The usual Doppler shifts in wavelength are also observed.

Discussion and Conclusions

The examples presented in this paper represent relatively low-frequency problems in which the wavelength of the incident sound is of the order of the characteristic dimension of the scattering body. For a rotorcraft application this would be typical of the first few harmonics of the main rotor blade-passage frequency (BPF) (of the order of 10 Hz) and the tail rotor fundamental BPF. The examination of relatively higher frequencies would increase the grid requirements. For example, consider a frequency of 250 Hz. The numerical methods used in this paper require at least 6 points per wavelength. This is equivalent to 5 grid points per meter for the 250-Hz sound wave. For a rotorcraft with dimensions $15 \times 4 \times 4$ m, the total grid requirements (incident plus scattered), assuming a uniform Cartesian grid, would be approximately 8×10^5 grid points. This would include a scattered field up to four wavelengths from the rotorcraft. This is of the same order as the grid used in the sphere scattering problem of the preceding section.

Also, the scattering bodies considered in this paper have been relatively smooth with no sharp corners. Chung and Morris,[12] using the total field version of the IMM, calculated the scattering of sound by a thin, finite, rigid plate. The plate was represented by an impedance mismatch region of one grid spacing, that is, two adjacent rows were assigned a lower mean density. The results compared very well with the numerical solution obtained by Tam and Dong[17] and the analytic solution. Thus it is expected that the present version of the IMM would be able to capture scattering by thin edges or wedge-shaped bodies.

In this paper a new method to simulate acoustic scattering has been introduced. Two- and three-dimensional simulations have been performed to find the limits and properties of the method. The method is found to make efficient, accurate predictions. No extra computations are required at the solid boundaries so that scattering by any complex geometry may be solved without additional computational time. In the future, the three-dimensional parallel code will be coupled to a rotorcraft noise prediction code to predict the noise generated by a rotor and scattered by a fuselage and wings.

Acknowledgments

This research was supported by NASA Langley Research Center under NASA Grant NAG-1-1924. The technical monitor is K. S. Brentner.

References

[1]Ffowcs Williams, J. E., and Hawkings, D. L., "Sound Generation by Turbulence and Surfaces in Arbitrary Motion," *Philosophical Transactions of the Royal Society of London Series A*, Vol. 264, No. 1151, 1969, pp. 321–342.

[2]Lighthill, M. J., "On Sound Generated Aerodynamically: I. General Theory," *Proceedings of the Royal Society of London Series A*, Vol. 211, No. 1107, 1952, pp. 564–587.

[3]Brentner, K. S., "Prediction of Helicopter Rotor Noise–A Computer Program Incorporating Realistic Blade Motions and Advanced Formulation," NASA TM-87721, 1986.

[4]Brentner, K. S., "An Efficient and Robust Method for Predicting Rotor High Speed Impulsive Noise," AIAA Paper 96-0151, Jan. 1996.

[5]Strawn, R., and Biswas, R., and Lyrintzis, A., "Helicopter Noise Predictions Using Kirchhoff Methods," *Proceedings of the American Helicopter Society, 51st Annual Forum. Part 1*, American Helicopter Society, Alexandria, VA, 1995, pp. 495–508.

[6]Brentner, K. S., and Farassat, F., "Analytical Comparison of Acoustic Analogy and Kirchhoff Formulation for Moving Surfaces," *AIAA Journal*, Vol. 36, No. 8, 1997, pp. 1379–1386.

[7]Hanson, D. B., and Magliozzi, B., "Propagation of Propeller Tone Noise Through a Fuselage Boundary Layer," *Journal of Aircraft*, Vol. 22, No. 1, 1985, pp. 63–70.

[8]Hanson, D. B., "Helicoidal Surface Theory for Harmonic Noise of Propellers in the Far Field," *AIAA Journal*, Vol. 18, No. 10, 1980, pp. 1213-1220.

[9]Atalla, N., and Glegg, S., "A Geometrical Acoustics Approach for Calculating the Effects of Flow on Acoustics Scattering," *Journal of Sound and Vibration*, Vol. 171, No. 5, 1994, pp. 681–694.

[10]Atalla, N., and Glegg, S., "Ray-Acoustics Approach to Fuselage Scattering of Rotor Noise," *Journal of the American Helicopter Society*, Vol. 38, No. 3, 1993, pp. 56–63.

[11]Chung, C., "Wave Propagation and Scattering in Computational Aeroacoustics," Ph.D. Dissertation, Dept. of Aerospace Engineering, Pennsylvania State Univ., University Park, PA, 1995.

[12]Chung, C., and Morris, P. J., "Acoustic Scattering from Two- and Three-Dimensional Bodies," *Journal of Computational Acoustics*, Vol. 6, No. 3, 1998, pp. 357–375.

[13]Tam, C. K. W., and Webb, J. C., "Dispersion-Relation-Preserving Difference Schemes for Computational Aeroacoustics," *Journal of Computational Physics*, Vol. 107, No. 2, 1993, pp. 262–281.

[14]Laik, O. A., "Direct Simulation of Acoustic Scattering by a Rotorcraft Surface and Flow," M.S. Thesis, Dept. of Aerospace Engineering, Pennsylvania State Univ., University Park, PA, 1998.

[15]Morris, P. J., "The Scattering of Sound from a Spatially-Distributed Axisymmetric Cylindrical Source by a Circular Cylinder," *Journal of the Acoustical Society of America*, Vol. 97, No. 5, 1995, pp. 2651–2656.

[16]Morris, P. J., "Scattering of Sound From a Spatially-Distributed, Spherically-Symmetric Source by a Sphere," *Journal of the Acoustical Society of America*, Vol. 98, No. 6, pp. 3536–3539.

[17]Tam, C. K. W., and Dong, Z., "Wall Boundary Conditions for High-Order Finite-Difference Schemes in Computational Aeroacoustics," *Theoretical and Computational Fluid Dynamics*, Vol. 6, No. 5-6, 1994, pp. 303–322.